Noname manuscript No.
(will be inserted by the editor)

Automatic Detection of the Intima-Media Thickness in Ultrasound Images of the Common Carotid Artery using Neural Networks

Rosa-María Menchón-Lara · María-Consuelo Bastida-Jumilla · Juan Morales-Sánchez · José-Luis Sancho-Gómez

Received: date / Accepted: date

Abstract Atherosclerosis is the leading underlying pathologic process that results in cardiovascular diseases, which represent the main cause of death and disability in the world. The atherosclerotic process is a complex degenerative condition mainly affecting the medium- and large-size arteries, which begins in childhood and may remain unnoticed during decades. The Intima-Media Thickness (IMT) of the Common Carotid Artery (CCA) has emerged as one of the most powerful tool for the evaluation of preclinical atherosclerosis. IMT is measured by means of B-mode ultrasound images, which is a non-invasive and relatively low cost technique. This paper proposes an effective image segmentation method for the IMT measurement in an automatic way. With this purpose, segmentation is posed as a pattern recognition problem and a combination of artificial neural networks has been trained to solve this task. In particular, Multi-Layer Perceptrons trained under the Scaled Conjugate Gradient algorithm have been used. The suggested approach is tested on a set of 60 longitudinal ultrasound images of the CCA by comparing the automatic segmentation with four manual tracings. Moreover, the intra- and inter-observer errors have also been assessed. Despite of the simplicity of our approach, several quantitative statistical evaluations have shown its accuracy and robustness.

Keywords Atherosclerosis · Ultrasound Imaging · Intima-Media Thickness · Pattern Recognition

R. M. Menchón-Lara · M. C. Bastida-Jumilla · Juan Morales-Sánchez · J. L. Sancho-Gómez
Dpto. Tecnologías de la Información y las Comunicaciones.
Universidad Politécnica de Cartagena.
Plaza del Hospital, 1. 30202, Cartagena (Murcia), Spain.
Tel.: +34-968-326542

R. M. Menchón-Lara
E-mail: rmml@alu.upct.es

M. C. Bastida-Jumilla
E-mail: consuelo.bastida@upct.es

J. Morales-Sánchez
E-mail: juan.morales@upct.es

J. L. Sancho-Gómez
E-mail: josel.sancho@upct.es

1 Introduction

CardioVascular Diseases (CVD) are the leading cause of death and disability in the world [33]. In 2008, about 17.3 million people died from CVD representing 30% of all global deaths. An important part of these were premature deaths and could have largely been prevented. Over 80% of CVD deaths take place in low- and middle-income countries and occur almost equally in men and women.

Atherosclerosis is responsible for a large proportion of CVD [33]. It is a chronic degenerative disease characterized by the accumulation of fatty material and cholesterol at the arterial walls. Therefore, atherosclerosis causes thickening and the reduction of elasticity in the arterial walls. Although this pathology may remain unnoticed for decades, atherosclerotic lesions (plaques) could even lead to a total occlusion of the blood vessels. This is the major underlying cause of heart attacks and strokes. For this reason, an early diagnosis and treatment of atherosclerosis are crucial to prevent patients from suffering more serious pathologies. In this sense, the Intima-Media Thickness (IMT) of the Common Carotid Artery (CCA) is considered as an early and reliable indicator of this condition [24, 42]. By studying IMT, a specialist can detect subclinical atherosclerosis and analyse the drug response.

The IMT is measured by means of a B-mode ultrasound scan, which is a non-invasive and low cost technique that allows a short time examination. The use of different protocols and the variability between observers is a recurrent problem in the measurement procedure [43]. The repeatability and reproducibility of the process is of great significance to analyse the IMT [3, 14].

The processing proposed in this work intends to improve and extend the manual measurement protocol used by the Radiology Department from Hospital Universitario Virgen de la Arrixaca [43]. IMT should be measured on the far (posterior) wall along a 1-cm-long section proximal to carotid bifurcation, where a bright-dark-bright pattern corresponding to the intima-media-adventitia layers of the arterial walls can be observed (see Fig. 1). The IMT is the distance between the lumen-intima (LI) interface and the media-adventitia (MA) interface. The physician manually takes three measurements in the selected carotid segment, and the measurement corresponding to the maximum IMT is considered the final value [43].

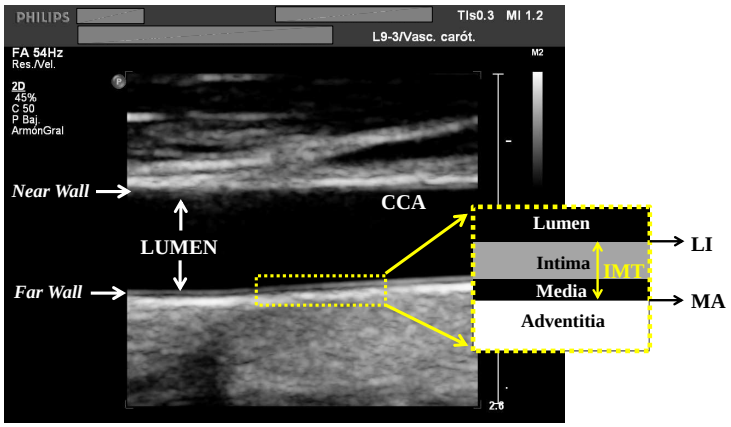

Fig. 1 Longitudinal view of CCA in an ultrasound B-scan image and scheme of the carotid interfaces for IMT measurement.

By means of image segmentation algorithms it is possible to reduce the subjectivity of manual approaches and detect the IMT throughout the artery length (not only in a few points), which leads to more precise results and allows to extract statistics of interest to the specialists. In the last two decades, several solutions have been developed to perform the carotid wall segmentation in ultrasound images [30]. Most of the proposed methods are not completely automatic and they require user interaction to start the algorithm, such as [22, 7, 40, 10, 35]. However, some fully automatic approaches were recently published [8, 12, 29, 1]. It is possible to make a classification of techniques according to the used methodology. In this sense, we can find algorithms based on edge detection and gradient-based techniques [22, 40, 10, 38], and other proposals based on dynamic programming [44, 21, 16, 6, 36, 20], active contours [7, 8, 5, 17, 25, 4, 37, 28] or in a combination of techniques [35, 23, 29]. We can also find highlight techniques based in statistical modeling [9, 19] and those in which Hough transform is employed [12, 46].

In this work, a segmentation technique based on the use of neural networks is proposed to extract and measure the IMT from a B-mode ultrasound scan image in an automatic way. Firstly, a given image is pre-processed to detect automatically the region of interest (ROI), which is the far wall of the vessel. Then, a network ensemble perform a classification of the pixels belonging to the ROI in either '*IMT-boundary*' pixels or '*non-IMT-boundary*' pixels, resulting to a binary output image. Finally, this binary image is post-processed to extract the final contours corresponding to the LI and MA interfaces in the most reliable sections for the IMT measurements.

The remainder of this paper is structured as follows. Sections 2.1 and 2.1 describe the set of tested ultrasound images and the reference segmentation results. In Sect. 2.3, the proposed segmentation method is explained in detail. The obtained results are shown in Sect. 3. Finally, a revision of the proposed method and the main extracted conclusions can be found in Sect. 4.

2 Materials and methods

2.1 Images Acquisition

A set of 60 longitudinal B-mode ultrasound images of the CCA, in DICOM format, have been used in the validation of our segmentation technique. All of them were provided by the Radiology Department of *Hospital Universitario Virgen de la Arrixaca* (Murcia, Spain). The subjects were 30 patients whose ages ranged from 25 to 79 years, with a mean age of 57 years, including 15 females and 15 males. Fig. 1 shows an example of the tested ultrasound images.

Ultrasound scans were acquired using a *Philips iU22 Ultrasound System* by means of three different ultrasound transducers (*L12-5*, *L9-3* and *L17-5*) according to the measurement protocol proposed in [43] and recorded digitally with 256 gray levels. The spatial resolution of the images ranges from 0.029 mm/pixel to 0.081 mm/pixel, with mean and standard deviation equal to 0.052 and 0.015 mm/pixel, respectively. The parameters of the scanner (depth of focus, frame rate, gain settings, log gain compensation) were adjusted in each case by the radiologist to obtain images with sufficient quality to correctly visualize the boundaries of the IMT. Some blurred and noisy images, affected by intraluminal artifacts, and some others with partially visible boundaries are included in the studied set.

The final objective of the proposed segmentation approach is to achieve a reliable automatic measurement of the IMT. The Mannheim consensus [42] recommends the performing

of the IMT measurement preferably on the far wall of the CCA within a region free of plaques, which provides increased accuracy, repeatability and reproducibility [14]. For this reason, ultrasound images with visible plaques are not included in our study. However, our method could be adapted to detect and characterize the different classes of plaques.

2.2 Manual Delineations

To assess the performance of the proposed segmentation method and the accuracy of the obtained IMT measurements, it is necessary to compare the automatic results with some indication of reference values (*ground-truth*). Although it is not possible to define the 'perfect segmentation', we use the average of four different manual segmentations to perform this comparison. In particular, two experienced radiologists delineated each one of the 60 ultrasound images twice, with a mean period of two months between tracings. Thus, a total of 240 manual segmentations have been performed. These reference values allow us the study of the inter-method differences (manual vs. automatic), and the intra- and inter-observer variability. Each manual segmentation of a given ultrasound image includes tracings for the lumen-intima interface and the media-adventitia interface on the far carotid wall. A simple routine developed under the Matlab environment assists the experts to do the manual delineations. By means of this application (see Fig. 2) it is possible to mark with the mouse so many points as it is wished on the image. These points are interpolated later to complete the required contours.

2.3 Segmentation Method

Fig. 3 shows an overview of the proposed IMT segmentation methodology. Firstly, a given ultrasound image of the CCA is pre-processed to automatically detect the region of interest (ROI). Then, a windowing process take place in order to construct the intensity pattern corresponding to each pixel. After this, a binary classification of the pixels on the ROI is performed. Finally, classification results are post-processed to extract the final contours for the LI and MA interfaces.

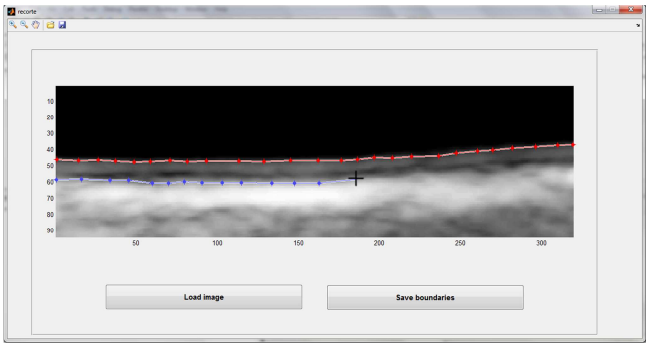

Fig. 2 Appearance of the application implemented in Matlab to assist in doing the manual segmentation of the carotid wall layers.

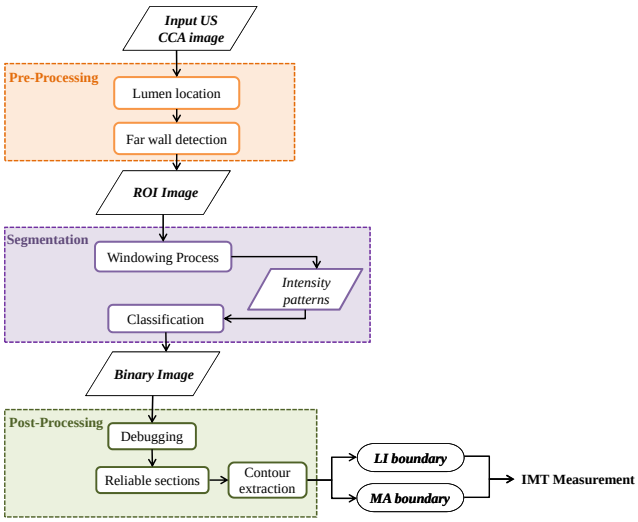

Fig. 3 Overview of the proposed methodology. It consists of three stages: Pre-Processing (detection of ROI), Segmentation (classification of pixels) and Post-Processing (extraction of final contours).

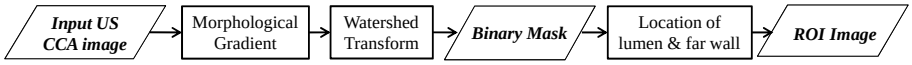

Fig. 4 Diagram of the pre-processing stage. First, a binary mask is created by means of Mathematical Morphology. Then, the dark area corresponding to the lumen is identified and the ROI (far wall) is selected.

2.3.1 Pre-processing Stage

In the ultrasound images (see Fig. 1), the lumen corresponds to a dark region (low echogenicity) delimited by the arterial walls. Over the lumen in the picture, at less depth, it is observed the echo corresponding to the near wall. The far wall, where the IMT is measured, is located below the lumen, and it constitutes our region of interest (ROI). This section describes a pre-processing stage in which the carotid far wall is located in a completely automatic way. Fig. 4 shows the main steps followed to reach this goal.

First of all, Watershed Transform [26] is applied to the morphological gradient of the image. The transformed image consists of a large number of watershed regions. Then, closed regions are filled by means of morphological operations [15, 13], resulting in a binary image. Only those objects with largest areas are extracted from this image to build a binary mask. Hereafter, an object in a binary image will refer to a set of white pixels connected by considering a 2D 8-connected neighbourhood. In this way, we avoid undesirable intra- and extra-luminal artifacts which can lead into error.

In the final binary mask, the largest black area connected to the biggest white object identifies the carotid lumen in the ultrasound image (see Fig. 5). Once the lumen has been located, we focus on its lower limit corresponding to the posterior wall of the CCA and the boundaries of the ROI are established. The superior boundary is fixed to 0.6 mm above the uppermost point of the far wall detected in the binary mask, whereas the bottom boundary is fixed to 1.5 mm below the lowest point. Thus, the size of the ROI is related to the carotid artery appearance in the ultrasound image.

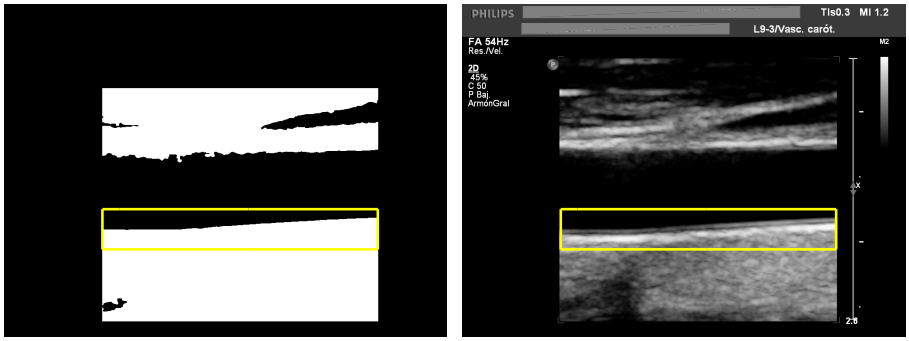

Fig. 5 ROI selection for the ultrasound image in Fig. 1: (left) Final binary mask with selected ROI; (right) Original image with superimposed ROI.

2.3.2 Classification Stage

Since segmentation can be considered as a classification of pixels, it is often treated as a pattern recognition problem and addressed with related techniques [34]. Besides, pattern recognition techniques provide the convenient flexibility and automation in medical image processing. This section describes the main step in the proposed application to measure the IMT, in which a neural network ensemble carries out the segmentation of the ultrasound images of the CCA.

The artificial neural networks used in this work are standard *Multi-Layer Perceptrons* (MLP), with a single hidden layer, trained under the *Scaled Conjugate Gradient* (SCG) learning rule [31]. Fig. 6 shows the configuration of the MLP used in this approach. The number of inputs depends on the size of the intensity patterns. In a similar way, the number of outputs depends on the size of the target vectors which is determined by the number of classes contemplated in the classification problem. However, the number of hidden neurons is a network parameter to be optimized.

The network takes as input information only the intensity values of the pixels from a neighbourhood of the pixel to be classified. Accordingly, a square window (W $\times$ W) must

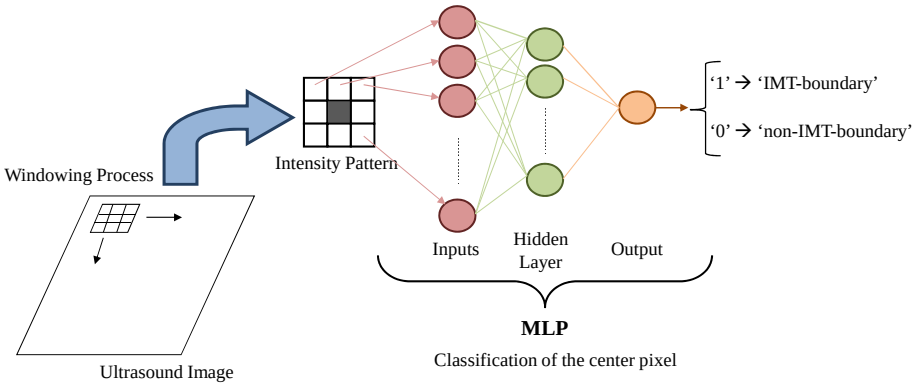

Fig. 6 Configuration of the MLP used in the segmentation procedure.

be shifted pixel-by-pixel over the input image (in our case, the ROI image). This window provides contextual information about the pattern of intensity values in the neighbourhood of the central pixel. The output layer consists of a single node, whose activation determines the class of the central pixel. The network is trained to produce a value of '1' for an input sub-image with a target '*IMT-boundary*' at its central position, and '0' otherwise ('*non-IMT-boundary*'). In our case, the networks were retrained 20 times with different initial random values of the connection weights. Besides, the number of hidden neurons is varied from 5 to 40. Thus, to complete the design of a given network, the training process is repeated 720 times (36×20). The optimal size of each network, i.e. the number of hidden neurons, is selected according to the minimum mean error reached on a validation dataset.

To perform the supervised neural network training, a labelled dataset is needed. In our case, this dataset was assembled by taking samples from five different manually segmented images. Finally, it consists of 8,000 patterns: 4,000 of them (50%) are from class '*IMT-boundary*', and the remaining (50%) are from class '*non-IMT-boundary*'. During the learning process, the dataset was randomly divided into three subsets: 60% of samples for training, 20% for validation (stopping criterion and network size selection) and 20% for testing. The test samples have been used in order to infer the network behaviour for new (unseen) ultrasound images. In this case, the prior probabilities of each class are the same in both the training and test data. Classification of the central pixel from an input pattern during test is simply determined by thresholding the network output. Only if the network output is greater than the threshold fixed to 0.5, the input will be classified as part of IMT (class '1'). Thus, a given input is assigned to the class with highest posterior probability [2].

In practice, complex classification problems require the contribution of several neural networks for achieving an optimal solution [27]. In the field of image processing, experimental results reported in the literature showed that the image classification accuracy provided by a network ensemble can outperform the accuracy of the best single net [11, 18, 45]. However, neural networks ensembles are effective only if the composing nets produce different errors. Several methods for the creation of ensembles of neural networks have been investigated. Such methods basically lie on varying the parameters related to the design and to the training of neural networks [11].

Following this idea, we propose a classification strategy in two stages to solve the posed segmentation task (see Fig. 7). Thus, the results from three different networks are combined by means of another neural network. In the first stage, each MLP is trained using a different window size to construct the input patterns (W = 3, 7, and 11, respectively). However, the number of inputs is equal to 9 for all these networks (central pixel and the eight pixels which define the limits of the corresponding window, as shown in Fig. 8). The reconstruction of the whole image (before thresholding) is needed at the output of each MLP in stage 1. Then, a new windowing process (with W = 3) is applied to each one of these images. The 3×3 neighbourhoods of corresponding pixels in the three output images of the first stage are assembled to construct the input patterns to the second classification stage. Thus, the single network in the second stage (MLP 4 in Fig. 7) consist of 27 inputs (9 from each output image of the first stage), one output and a number of hidden nodes optimized by means of the validation error.

A complete study of the individual response of the networks according to the size of the considered neighbourhood, i.e. depending on W, is detailed in Sect. 3.1. Moreover, Sect. 3.1 also includes results from the searching process of the best combination of MLP and justifies the selection of the configuration proposed in Fig. 7.

Figs. 10 to 13 show the partial and final classification results for the ultrasound image in Fig. 1, according to the proposed classification scheme. As can be seen, depending on the

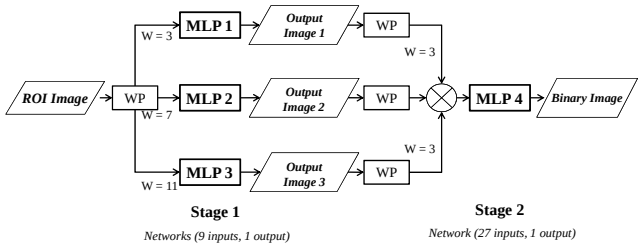

Fig. 7 Network ensemble strategy adopted to solve the segmentation task. In Figure, WP denotes 'Windowing Process'.

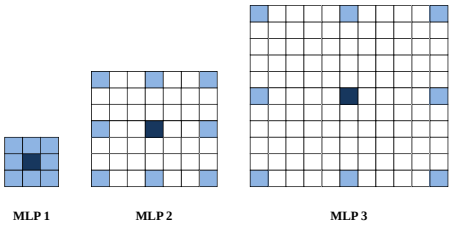

Fig. 8 Input features selected for each MLP in Fig. 7.

considered window size, the networks in the first stage lead to different classification errors (Figs. 10-12). As the value of W increases, the network tends to produce thicker but more definite boundaries and to reduce the classification errors outside the LI and MA interfaces. The combination of networks in the second stage allows to obtain a cleaner image (Fig. 13), in which the classification errors of pixels are greatly reduced. Nevertheless, it is still necessary to eliminate some residues, to refine the contours and to separate the interfaces. To this end, a post-processing stage has been designed (detailed in Sect. 2.3.3).

2.3.3 Post-processing Stage

The output binary image of the classification stage should be debugged and refined to measure the IMT in order to identify and discard the false positive classification errors (see Fig. 13). For this purpose, the post-processing stage shown in Fig. 15 is applied to the classification results.

To begin with, it is necessary to identify and separate the LI and MA interfaces. With this aim, the image is processed, column by column, looking for reliable columns. Therefore, we reject: (*i*) columns in which all the pixels have '0' value; (*ii*) those columns where a single boundary has been found; (*iii*) columns wherein two objects are detected and the separation between them is considered atypical. Note that the case in which the column is composed of more than two objects has still not been taken into account. At this point, we apply a hard constraint to ensure the location of the optimal sections to measure the IMT. In those columns which have not been discarded, the distance (number of pixels) between the found objects is assessed. Then, we consider that a change over 40% relative to the average of this distance is not valid and we discard those columns that do not fulfil this condition. This value has been taken because all the available images provided by the hospital are free of plaques. Thus, there are not large variations in the separation of interfaces within the same ultrasound image. Moreover, in columns with more than two detected objects, this constraint helps us to

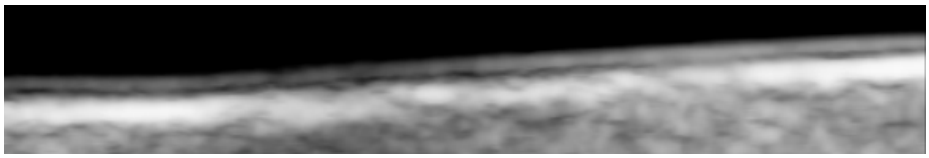

Fig. 9 ROI for the ultrasound image in Fig. 1.

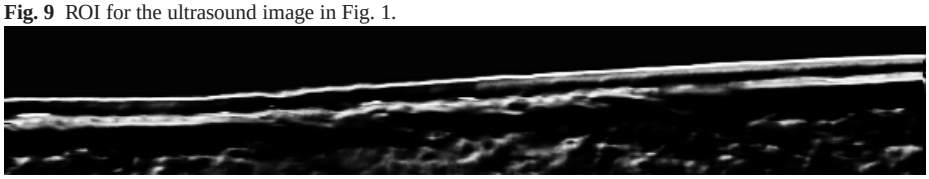

Fig. 10 Partial result of the first classification stage corresponding to 'MLP 1' for the ROI image in Fig. 9 ('*Output Image 1*' in Fig. 7).

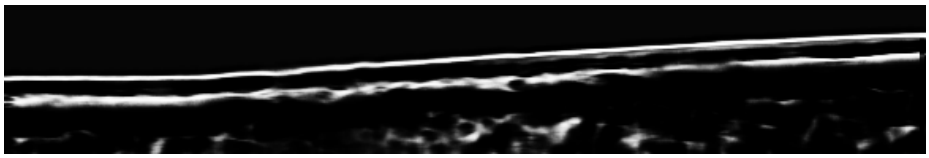

Fig. 11 Partial result of the first classification stage corresponding to 'MLP 2' for the ROI image in Fig. 9 ('*Output Image 2*' in Fig. 7).

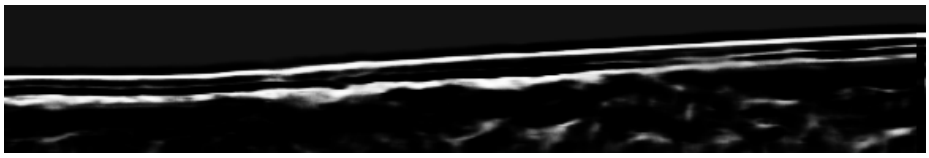

Fig. 12 Partial result of the first classification stage corresponding to 'MLP 3' for the ROI image in Fig. 9 ('*Output Image 3*' in Fig. 7).

Fig. 13 Binary image obtained at the output of the second classification stage.

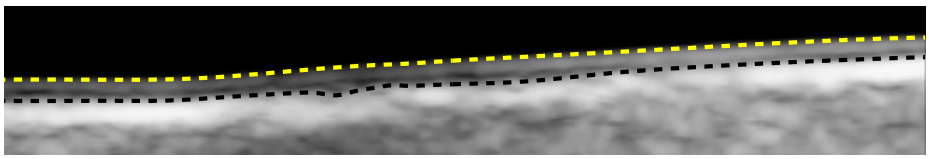

Fig. 14 Final LI and MA boundaries obtained after the post-processing stage for the binary image in Fig. 13.

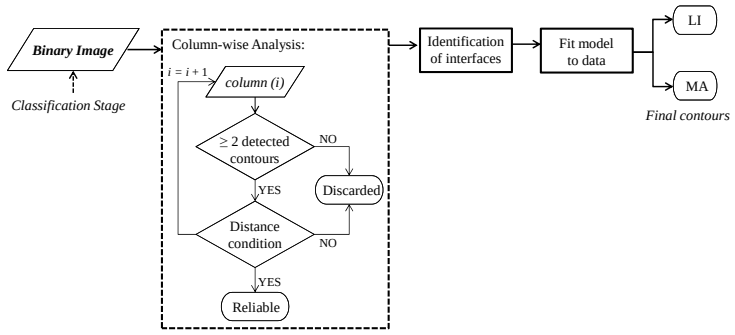

Fig. 15 Diagram of the post-processing stage. First, the classification results are debugged and, then, the LI and MA interfaces are identified.

identify the correct ones. The reliable sections for the IMT measurement, i.e. groups of not discarded consecutive columns, are obtained in this way. In these sections, pixels belonging to the LI interface (upper) and MA interface (bottom) are identified.

Once the measurement sections have been located, we must consider another aspect about the classification results. Due to the poor resolution of the ultrasounds, we obtain thick boundaries instead of one-pixel contours. This happens because the networks find the searched intensity patterns, since they have been trained for it, in all these pixels. In order to define the final contours on which the IMT measurement is performed, we formulate a nonlinear least squares problem by fitting a sum of Gaussian models (up to 5 models) to the data and it is solved using the Trust-Region Reflective algorithm [32]. By that means, the best model, which minimizes the Root Mean Squared Error (RMSE) between the white pixels in the binary image and the approximated contour, is found for each interface. Fig. 14 shows the final contours for the LI and MA interfaces extracted from the binary image in Fig. 13.

3 Results and discussion

The suggested method was developed and tested under Matlab, on a PC with an Intel Core i5 processor at 2.8 GHz and a 8 GB RAM. The mean total CPU time per processed image is 3.44 s. The ROI selection task (pre-processing stage) has showed a high efficiency by spending 0.34 s in mean for each case. Once the networks have been trained, classification results are provided in a fast way, with an average response time of 0.72 s for all the pixel in the selected ROI. On the other hand, given the binary output image of an ultrasound image, the post-processing stage achieves the location of the reliable sections and returns the final IMT boundaries in 2.4 s (mean time).

In this section, the performance and accuracy of the proposed methodology from different points of view are characterized. Sect. 3.1 presents an exhaustive analysis of the networks performance. In Sect. 3.2 a visual validation of the results for several images is shown. The degree of agreement between manual and automatic segmentations is included in Sect. 3.3. Sect. 3.4 closes the analysis of the results with a study of the variability in the IMT measurements.

3.1 Networks Performance

In this section, the configuration of neural networks proposed in Sect. 2.3.2 to solve the segmentation task is justified (see Fig. 7). First, a performance study of a single MLP was realized for different window sizes (W from 3 to 21) by assuming, in each case, the selection of 9 input features shown in Fig. 8. For this analysis, the *accuracy* (ACC), *specificity* (SPEC) and *sensitivity* (SEN) of the binary classification were assessed on the test set in the following form:

$$ACC(\%) = 100 \times \frac{TP + TN}{TP + TN + FP + FN} \tag{1}$$

$$SPEC(\%) = 100 \times \frac{TN}{TN + FP} \tag{2}$$

$$SEN(\%) = 100 \times \frac{TP}{TP + FN} \tag{3}$$

where TP is the number of true positives; TN is the number of true negatives; FP and FN are the number of false positives and false negatives, respectively. Thus, ACC represents the success rate, SPEC relates to the ability to identify negative results ('*non-IMT-boundary*' pixels) and SEN relates to the ability to identify positive results ('*IMT-boundary*' pixels). Since the networks were retrained 20 times with different initial conditions, the results are shown in terms of mean and standard deviation (SD).

Table 1 shows the response of a single network according to the value of W. As can be seen, the accuracy stagnates for W greater than 11. Moreover, for W $\geq$ 13 the specificity drops considerably due to the increase of false positives. This FP increase is translated into dirtier images at the network output. Therefore, it is possible to conclude that the best single MLP is the one that considers the pixel intensities of a 11$\times$11 neighbourhood of the pixel to be classified. These results are also shown graphically in Fig. 16 to facilitate its analysis.

Nevertheless, these results can be improved by means of the combination of different networks. Thus, a network ensemble is proposed in this work to solve the segmentation of the ultrasound images of the CCA. In this sense, a study of all the possible combinations of MLP has been performed to find the best configuration for our specific application. Basing on the conclusions extracted from Table 1 and Fig. 16, only the networks with W from 3 to 11 were considered in this analysis. As commented in Sect. 2.3.2, the combination of MLP is performed by other MLP. Thus, the classification of pixels is performed in two stages. Once the output images of the networks in the first stage are obtained, a new windowing

Table 1 Single MLP performance for different neighbourhood sizes. Mean $\pm$ SD values.

	ACC (%)	SPEC (%)	SEN (%)
W = 3	87.10 $\pm$ 0.72	83.67 $\pm$ 1.06	90.53 $\pm$ 0.58
W = 5	90.28 $\pm$ 0.58	86.62 $\pm$ 0.84	93.94 $\pm$ 0.57
W = 7	91.59 $\pm$ 0.80	88.06 $\pm$ 1.08	95.13 $\pm$ 0.79
W = 9	91.91 $\pm$ 0.62	89.10 $\pm$ 1.00	94.71 $\pm$ 0.53
W = 11	92.17 $\pm$ 1.00	89.55 $\pm$ 1.63	94.79 $\pm$ 0.57
W = 13	92.62 $\pm$ 0.45	88.99 $\pm$ 0.71	96.24 $\pm$ 0.53
W = 15	92.05 $\pm$ 0.51	88.15 $\pm$ 0.72	95.96 $\pm$ 0.48
W = 17	91.93 $\pm$ 0.62	87.64 $\pm$ 0.72	96.22 $\pm$ 0.69
W = 19	92.19 $\pm$ 0.59	87.69 $\pm$ 0.54	96.69 $\pm$ 0.77
W = 21	91.91 $\pm$ 0.54	86.98 $\pm$ 0.51	96.85 $\pm$ 0.85

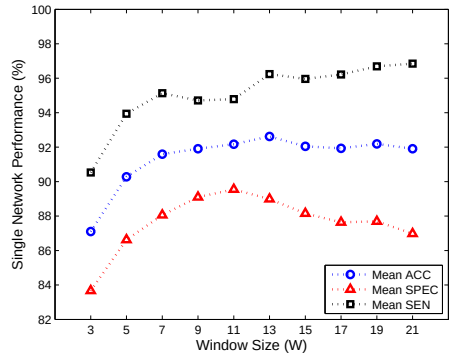

Fig. 16 Network performance for different window sizes (mean values). For W $\geq$ 13 SPEC drops considerably. Thus, the best configuration corresponds to a 11×11 neighbourhood.

process (with W = 3) is carried out to assemble the input patterns to the MLP in the second stage.

Table 2 shows the performance of all the possible combinations of two MLP. The analysis of all the possible combinations of three MLP is shown in Table 3. On the other hand, Table 4 includes the corresponding results for the combination of four MLP and the combination of all the considered MLP. In each case, the grey table cells indicate the combined networks. The results are sorted from highest to lowest accuracy. Obviously, the best results are obtained when the best single network (W = 11) is included.

Fig. 17 graphically shows a comparison of the best configurations. The best single network (W = 11), the best combination of two, three and four MLP and the combination of all the networks (W from 3 to 11) are included. In all the cases, it is possible to verify how the combination of MLP overcomes to the best single network. As can be observed in the left graph, there are no significant differences between the best combinations of networks in terms of mean ACC, which is about 94.4% in all the cases. For this reason, the optimal network ensemble must be chosen according to the best relationship between SEN and SPEC for our particular application. In this sense, the combinations of three and five MLP show a slight improvement. Moreover, the graph on the right depicts the best cases (highest ACC from 20 initiations) of the different configurations, where the case of 3 MLP stands out again. Thus, it is possible to conclude that the best configuration for our application is the combination of three MLP with W values equal to 3, 7 and 11.

3.2 Automatic Segmentation Examples

As commented in Sect. 2.1, the proposed segmentation method has been tested on a set of 60 B-mode ultrasound images of the CCA provided by the Radiology Department of Hospital Universitario Virgen de la Arrixaca. Some examples of segmented images are shown in this section. The final boundaries corresponding to the LI and MA interfaces detected by our automatic segmentation method are superimposed on the ultrasounds.

To ensure an optimal visualization of the interfaces in the ultrasound, a straight and horizontal appearance of the carotid artery in the image is desirable. However, this projection is not always possible. Sometimes, the CCA may be tilted or curved because of the probe position or the own anatomy of the subject. In the case of algorithms using human interaction,

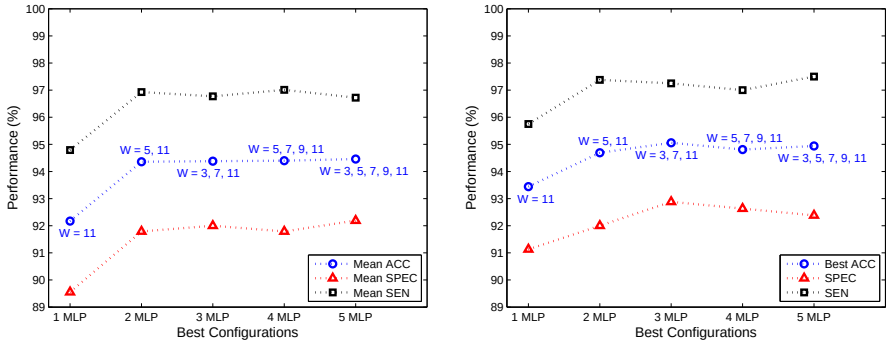

Fig. 17 Performance of the best studied configurations: (left) Mean values; (right) Best cases.

the operator can select the optimal area of the image for the IMT measurement. Nevertheless, totally automatic methods must be robust against the morphology of the artery.

When the visualization of the artery in the image is the ideal one, i.e. straight and quasi-horizontal, our segmentation reaches highly accurate results without major complications (see Fig. 14). Furthermore, it proves to be robust against the orientation and appearance of the CCA in the image without being necessary to realize any correction in this sense during the pre-processing stage. Fig. 18 depicts the good segmentation results of a CCA that is inclined with respect to the image edges. The capability of our method in dealing arteries with certain curvature is shown in Fig. 19.

The utilization of different window sizes and the combination of the corresponding networks allow the adaptation of our algorithm to images with different spatial resolution. Fig. 20, with a substantial variation with respect to the other ones in the image resolution, is included as evidence of this fact. Moreover, Fig. 21 shows the particular case in which the LI interface is only partially visible, whereas Fig. 22 evidences the good response of our method even if the carotid bulb appears in the image.

Table 2 Performance of all the possible combinations of two MLP. Mean and SD values (%). The results are sorted from highest to lowest ACC.

3×3	■		■	■	■	■			■	
5×5		■	■	■	■		■	■		■
7×7	■	■		■		■	■			■
9×9	■	■	■					■	■	■
11×11					■	■	■	■	■	■
ACC_{mean}	94.36	94.24	94.12	93.95	93.52	93.28	93.18	92.65	92.65	91.33
ACC_{SD}	0.23	0.25	0.22	0.28	0.18	0.26	0.20	0.25	0.30	0.31
$SPEC_{mean}$	91.79	91.98	91.33	91.52	90.26	90.25	90.61	89.86	89.45	88.37
$SPEC_{SD}$	0.43	0.43	0.44	0.38	0.38	0.52	0.39	0.46	0.50	0.66
SEN_{mean}	96.93	96.50	96.90	96.38	96.78	96.31	95.76	95.44	95.84	94.29
SEN_{SD}	0.32	0.40	0.34	0.50	0.29	0.55	0.37	0.27	0.30	0.38

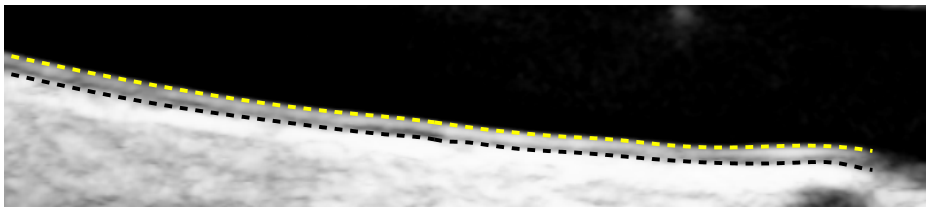

Fig. 18 Example of good segmentation on a tilted carotid artery: ROI [137 $\times$ 728]. The image resolution is 0.050 mm/pixel and the automatic measure of the IMT_{MAD} is 0.568 mm.

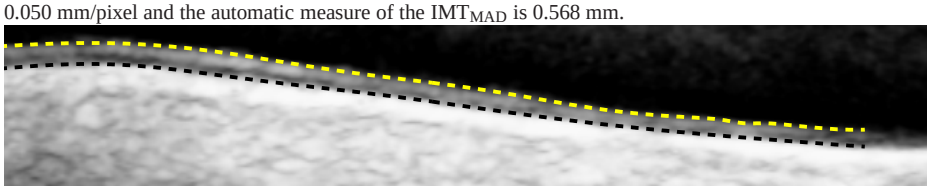

Fig. 19 Example of good segmentation on a curved carotid artery: ROI [111 $\times$ 747]. The image resolution is 0.047 mm/pixel and the automatic measure of the IMT_{MAD} is 0.619 mm.

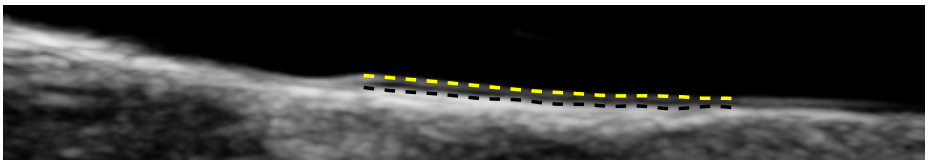

Fig. 20 Example of robustness against changes in spatial resolution: ROI [79 $\times$ 466]. The image resolution is 0.081 mm/pixel and the automatic measure of the IMT_{MAD} is 0.456 mm.

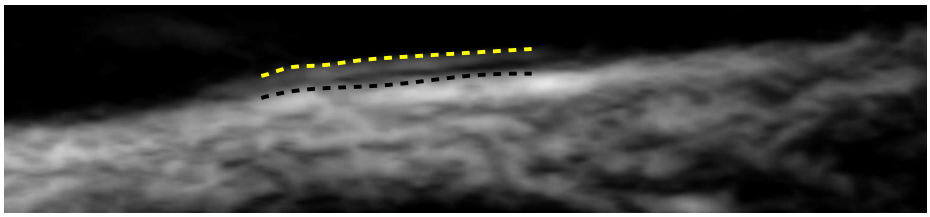

Fig. 21 Example of good segmentation when the LI interface is partially visible: ROI [142 $\times$ 734]. The image resolution is 0.033 mm/pixel and the automatic measure of the IMT_{MAD} is 0.546 mm.

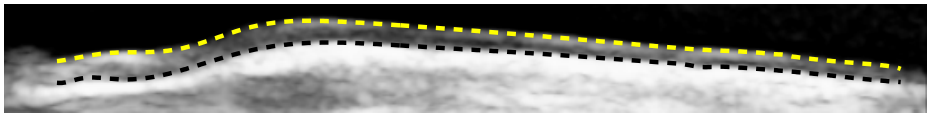

Fig. 22 Example of good segmentation when the carotid bulb is visible: ROI [65 $\times$ 572]. The image resolution is 0.066 mm/pixel and the automatic measure of the IMT_{MAD} is 0.758 mm.

Table 3 Performance of all the possible combinations of three MLP. Mean and SD values (%). The results are sorted from highest to lowest ACC.

3×3	■	□	□	■	■	□	□	■	■	■
5×5	□	■	■	■	□	□	■	□	■	■
7×7	■	■	□	□	□	■	■	■	□	■
9×9	□	□	■	□	■	■	■	■	■	□
11×11	■	■	■	■	■	■	□	□	□	□
ACC_{mean}	94.38	94.31	94.25	94.23	94.18	94.16	93.77	93.68	93.39	92.59
ACC_{SD}	0.32	0.26	0.27	0.22	0.26	0.20	0.26	0.19	0.34	0.30
$SPEC_{mean}$	92.00	91.39	91.62	91.83	91.93	91.46	90.56	90.98	90.88	89.97
$SPEC_{SD}$	0.64	0.38	0.50	0.48	0.48	0.37	0.54	0.38	0.48	0.58
SEN_{mean}	96.77	97.23	96.88	96.63	96.44	96.86	96.98	96.38	95.90	95.21
SEN_{SD}	0.49	0.33	0.36	0.39	0.39	0.32	0.27	0.44	0.47	0.34

Table 4 Performance of all the possible combinations of four and five MLP. Mean and SD values (%). The results are sorted from highest to lowest ACC.

3×3	■	□	■	■	■	■
5×5	■	■	■	□	■	■
7×7	■	■	□	■	□	■
9×9	■	■	■	■	■	■
11×11	■	■	■	■	■	□
ACC_{mean}	94.46	94.40	94.31	94.30	94.29	93.72
ACC_{SD}	0.25	0.23	0.29	0.30	0.29	0.34
$SPEC_{mean}$	92.19	91.79	91.95	91.84	91.94	91,00
$SPEC_{SD}$	0.43	0.45	0.61	0.50	0.72	0.49
SEN_{mean}	96.72	97.01	96.66	96.76	96.64	96.44
SEN_{SD}	0.42	0.35	0.38	0.44	0.49	0.43

3.3 Segmentation Accuracy

In order to validate the segmentation results, the automatically obtained contours have been compared with four manual tracings performed by two different expert radiologists. Therefore, a total of 240 manual segmentations have been performed. These comparisons were carried out separately for the LI and MA interfaces using different metrics: Mean Absolute Distance (MAD), Poly-Line Distance (PLD) and Center Line Distance (CLD). Hereafter, we will refer to the different segmentations as follows:

- $M1_1$: First manual segmentation from expert no. 1.
- $M1_2$: Second manual segmentation from expert no. 1.
- M1: Average contour from expert no. 1, i.e. mean ($M1_1$, $M1_2$).
- $M2_1$: First manual segmentation from expert no. 2.
- $M2_2$: Second manual segmentation from expert no. 2.
- M2: Average contour from expert no. 2, i.e. mean ($M2_1$, $M2_2$).
- GT: (Ground-Truth) Average of the four manual tracings.
- A: Our automatic segmentation.

On the one hand, the intra-observer error is assessed in each case by comparing two manual segmentations from the same expert ($M1_1$-$M1_2$ and $M2_1$-$M2_2$). Furthermore, the inter-observer error between the average contours from each expert was also computed (M1-M2). By means of these errors, the uncertainty and variability of the manual procedure are characterized. On the other hand, the inter-method error was evaluated by comparing our automatic segmentations with those considered as ground-truth (A-GT).

MAD is the most used quantitative metric to evaluate IMT and the accuracy of a segmentation method. It is based on the vertical distance between contours along the longitudinal axis of an image. Given two boundaries (B_1 and B_2), MAD is defined as:

$$MAD(B_1, B_2) = \frac{1}{N} \sum_{y=1}^{N} |B_1(y) - B_2(y)| \tag{4}$$

where N is the number of points constituting the two boundaries, and y is the index spanning the columns of the image. Nevertheless, MAD may deviate from the true distance between two contours when these present certain slope or curvature.

Poly-Line Distance was proposed in [41] as a more robust and reliable indicator of the distance between two boundaries. In this case, it is not a necessary condition that two contours have the same number of points. Given B_1 with N_1 points and B_2 with N_2 points (see Fig. 23), PLD between B_1 and B_2 is defined as:

$$PLD(B_1, B_2) = \frac{d(B_1, B_2) + d(B_2, B_1)}{N_1 + N_2} \tag{5}$$

where $d(B_1, B_2)$ is the distance between the vertices of B_1 to the corresponding closest segments of B_2 and it is computed as:

$$d(B_1, B_2) = \sum_{v \in B_1} d(v, B_2) \tag{6}$$

and $d(B_2, B_1)$ is assessed in a similar manner.

PLD from $v \in B_1$ to B_2 is defined as $d(v, B_2) = \min_{s \in B_2} d(v, s)$, where s is the segment of B_2 from v_1 to v_2. The distance $d(v, s)$ is evaluated as:

$$d(v, s) = \begin{cases} | \, d_\perp \, |, \text{ if } 0 \leq \lambda \leq d_{12} \\ \min(d_1, d_2), \text{ otherwise} \end{cases} \tag{7}$$

where d_1, d_2 and d_{12} are the Euclidean distances between the points v and v_1, between v and v_2, and between v_1 and v_2, respectively:

$$d_1 = \sqrt{(x - x_1)^2 + (y - y_1)^2} \tag{8}$$

$$d_2 = \sqrt{(x - x_2)^2 + (y - y_2)^2} \tag{9}$$

$$d_{12} = \sqrt{(x_2 - x_1)^2 + (y_2 - y_1)^2} \tag{10}$$

As can be seen in Fig. 23, $d_\perp$ is the normal distance between v and the segment s, and λ is the distance along the vector of the segment s:

$$d_\perp = \frac{(y_2 - y_1)(x_1 - x) + (x_2 - x_1)(y - y_1)}{\sqrt{(x_2 - x_1)^2 + (y_2 - y_1)^2}} \tag{11}$$

$$\lambda = \frac{(y_2 - y_1)(y - y_1) + (x_2 - x_1)(x - x_1)}{\sqrt{(x_2 - x_1)^2 + (y_2 - y_1)^2}} \tag{12}$$

CLD [39] is based on the calculation of the center line between the two boundaries to compare. Once this line is found, a segment perpendicular to the center line, which intersects

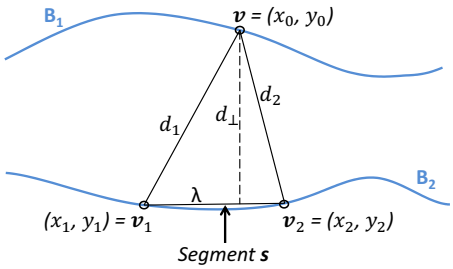

Fig. 23 Diagram of the Poly-Line Distance metric between two boundaries.

with B_1 and B_2, is considered at each point. Finally, CLD is defined as the mean length of all the segments:

$$CLD(B_1, B_2) = \frac{1}{N}\sum_{i=1}^{N} l_i \tag{13}$$

where l_i is the length of the *i-th* segment and N is the number of points of the center line. CLD, as PLD, takes into account the local orientation of the boundaries. However, just like in the MAD metric, the number of points in B_1 and B_2 must be the same.

Once the distance metrics have been defined, we are able to analyse the obtained results. Tables 5 and 6 show the mean and standard deviation values (over the 60 tested ultrasound images) of the segmentation error for the LI and MA interfaces, respectively. The MAD, PLD and CLD metrics are used to assess the variations between analogous contours (LI or MA) from two different segmentations.

Fig. 24 shows the distributions of MAD, PLD and CLD metrics for the intra-observer errors, whereas Figs. 25 and 26 depict the inter-observer and the inter-method error, respectively. The box whiskers extend to the most extreme not outliers values (marked as $*$). On each box, the three horizontal lines represent the 25^{th} percentile, the median and the 75^{th} percentile of the data. These values are also shown in Table 7.

The distributions of the intra-observer segmentation errors reveal that a greater variability exists for the MA interface. This is due to the fact that, in general, transitions from lumen to intima layer are clearer than transitions from media to adventitia layer. The same trend, i.e. the major uncertainty for MA, can be seen in the inter-observer segmentation error. However, when the comparisons are made between our automatic contours and the GT, the MA segmentation error is considerably reduced. Thus, the proposed method improves the segmentation of the interface most difficult to recognize, even for the human visual system.

Table 5 Segmentation error for the lumen-intima interface in µm. Mean and standard deviation for the 60 images using MAD, PLD and CLD metrics.

Mean ± SD	LUMEN-INTIMA INTERFACE		
n = 60	MAD	PLD	CLD
$M1_1$-$M1_2$	32.28 ± 14.51	34.07 ± 14.85	32.24 ± 14.65
$M2_1$-$M2_2$	36.29 ± 12.96	39.24 ± 13.67	35.85 ± 13.02
M1-M2	30.08 ± 13.11	33.11 ± 16.86	30.26 ± 14.49
A-GT	37.03 ± 18.57	39.62 ± 18.14	37.03 ± 18.45

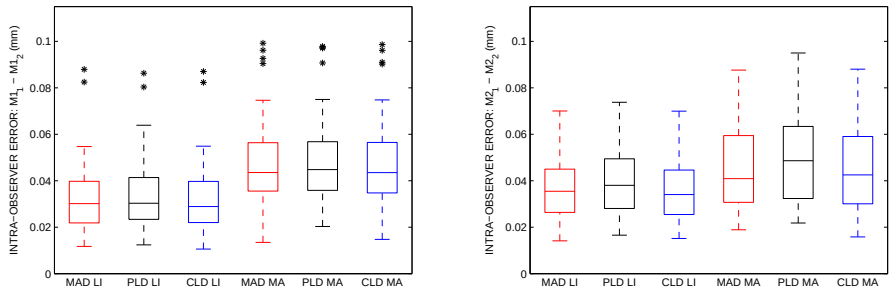

Fig. 24 Intra-observer segmentation error. Box plots of MAD, PLD and CLD (mm) for LI and MA. (left) $M1_1$-$M1_2$; (right) $M2_1$-$M2_2$.

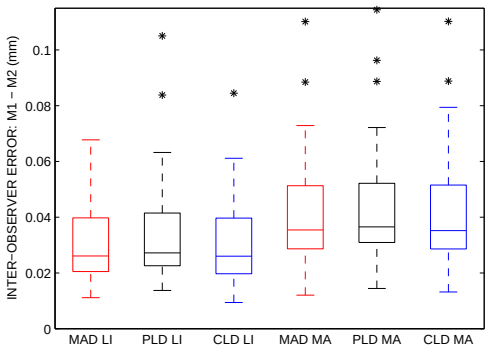

Fig. 25 Inter-observer segmentation error (M1-M2). Box plot of MAD, PLD and CLD (mm) for LI and MA.

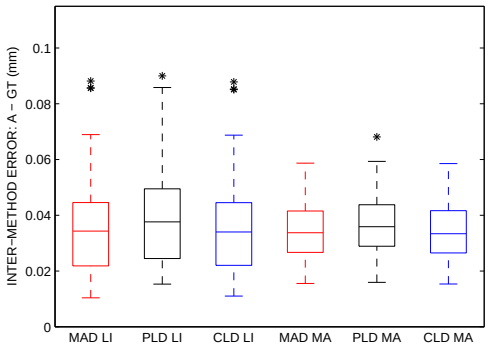

Fig. 26 Inter-method segmentation error (A-GT). Box plot of MAD, PLD and CLD (mm) for LI and MA.

Besides, the segmentation error (A-GT) of the LI interface is comparable to the intra- and inter-observer errors between manual segmentations.

Despite the greater error and the higher dispersion of the error for the MA boundaries, there is a good agreement between manual tracings. Thus, for LI interfaces: 26.1 μm $\leq$ median (MAD) $\leq$ 35.5 μm; 27.2 μm $\leq$ median (PLD) $\leq$ 38 μm; and 26 μm $\leq$ median (CLD) $\leq$ 34 μm. On the other hand, the error between manual MA interfaces is: 35.4 μm $\leq$ median (MAD) $\leq$ 43.5 μm; 36.5 μm $\leq$ median (PLD) $\leq$ 48.6 μm; and 35.2 μm $\leq$ median (CLD) $\leq$ 43.5 μm. These values emphasise the goodness of the manual segmentations.

3.4 IMT Measurements

Given an ultrasound image and two different segmentations (S_1 and S_2) to compare, the degree of agreement between its IMT measures is assessed by calculating the absolute error value:

$$\epsilon^{IMT_i} = |IMT_i^{S_1} - IMT_i^{S_2}| \tag{14}$$

being ϵ^{IMT_i} the IMT measurement error between the segmentation S_1 and the segmentation S_2 for the *i-th* image. In each case, the IMT value, i.e. the distance between the boundaries corresponding to LI and MA, is evaluated by using the aforementioned metrics: MAD, PLD and CLD.

The mean and standard deviation values (60 processed images) for the intra-observer, inter-observer and inter-method IMT measurement errors can be seen in Table 8. The mean absolute error of the automatic measurements is about 37 μm, which is a similar value (slightly lower) to the inter-observer error. In addition, the correlation coefficients (R) between the automatic measures and the GT are comparable to the R values associated with the intra-observer variability. Therefore, the precision in the automatic IMT measurements is full well justified. Moreover, Table 9 shows the mean absolute error reached by other methods. However, a complete comparison with other proposed techniques is not possible because each one is characterized by means of the average values of the error on its own image dataset considering a particular ground-truth. Furthermore, most are not fully automatic and these methods consider a single image resolution or only permit a minimal variation of this parameter. Thus, the goodness of our method can only be understood by comparing with the intra- and inter-observer errors.

Besides, the statistical distribution of the IMT measurement errors between different segmentations is depicted in the box plot of the Fig. 27. As can be seen, there is not meaningful differences in the statistical distribution of the measurement error when the metric used in the evaluation of IMT is MAD, PLD or CLD. Because of this fact, only the IMT measures assessed by PLD metric are considered hereinafter.

Table 6 Segmentation error for the media-adventitia interface in μm. Mean and standard deviation for the 60 images using MAD, PLD and CLD metrics.

Mean $\pm$ SD	MEDIA-ADVENTITIA INTERFACE		
n = 60	MAD	PLD	CLD
$M1_1$-$M1_2$	47.31 $\pm$ 18.29	48.76 $\pm$ 18.34	47.26 $\pm$ 18.31
$M2_1$-$M2_2$	46.34 $\pm$ 19.25	49.01 $\pm$ 19.05	46.06 $\pm$ 19.18
M1-M2	41.47 $\pm$ 18.47	43.53 $\pm$ 19.44	41.46 $\pm$ 18.66
A-GT	34.52 $\pm$ 10.29	37.02 $\pm$ 11.23	34.67 $\pm$ 10.68

Table 7 Segmentation error statistics for the LI and MA interfaces in µm.

		First Quartile			Median			Third Quartile		
		MAD	PLD	CLD	MAD	PLD	CLD	MAD	PLD	CLD
$M1_1$-$M1_2$	LI	21.84	23.36	21.99	30.14	30.29	28.90	39.76	41.38	39.70
	MA	35.53	35.85	34.74	43.53	44.81	43.51	56.38	56.69	56.51
$M2_1$-$M2_2$	LI	26.38	28.05	25.45	35.48	38.02	34.04	45.00	49.46	44.61
	MA	30.71	32.36	30.06	40.91	48.61	42.50	59.46	63.37	59.06
M1-M2	LI	20.49	22.57	19.72	26.09	27.18	26.00	39.74	41.47	39.68
	MA	28.63	30.93	28.60	35.42	36.54	35.18	51.31	52.16	51.54
A-GT	LI	21.82	24.46	22.03	34.32	37.63	33.99	44.56	49.47	44.53
	MA	26.70	28.87	26.49	33.72	35.91	33.38	41.53	43.77	41.64

Figs. 28 to 31 establish the statistical evaluation of IMT for the manual and the automatic segmentations. The right figures show the linear regression analysis for the IMT between different segmentations; whereas the Bland-Altman plots of the differences between the IMT of the corresponding two segmentations against their average can be seen at left figures.

The regression analyses between manual segmentations from the same expert (Figs. 28 and 29 (right)) show high correlation coefficients ($0.984 \leq R \leq 0.986$). Besides, the inter-observer reproducibility of the IMT measurement is 96.5%, see the correlation coefficients in Table 8 and Fig. 30 (right). Furthermore, when comparing the automatic measures with the GT (Fig. 31 (right)), we also obtain a high degree of agreement between methods ($R \geq$ 98%). Bland-Altman plots show the following limits of agreement (mean $\pm$ 2 $\times$ standard deviation): -4 $\pm$ 66 µm between $M1_1$ and $M1_2$, 7 $\pm$ 71 µm between $M2_1$ and $M2_2$, 11 $\pm$ 103 µm for the inter-observer variability, -26 $\pm$ 72 µm between A and GT. Therefore, the proposed method tends to slightly underestimate the IMT. Even so, the lower limit of agreement between automatic measurements and the GT (-97 µm) is similar to that of the

Table 8 IMT measurement errors (mean and standard deviation values in µm) and correlation coefficients (%) between different segmentations.

	IMT_{MAD}		IMT_{PLD}		IMT_{CLD}	
	ϵ^{IMT} (µm)	R (%)	ϵ^{IMT} (µm)	R (%)	ϵ^{IMT} (µm)	R (%)
$M1_1$-$M1_2$	27.79 $\pm$ 19.53	98.52	27.05 $\pm$ 18.92	98.57	27.11 $\pm$ 18.77	98.58
$M2_1$-$M2_2$	28.87 $\pm$ 22.08	98.43	28.67 $\pm$ 22.88	98.41	28.83 $\pm$ 22.04	98.40
M1-M2	37.84 $\pm$ 37.66	96.43	37.19 $\pm$ 36.87	96.49	37.23 $\pm$ 36.71	96.51
A-GT	37.63 $\pm$ 25.18	98.17	36.70 $\pm$ 24.29	98.20	36.83 $\pm$ 24.50	98.24

Table 9 Performance of other techniques for IMT measurement. n indicates the number of tested ultrasound images. The metric adopted to assess the IMT measurement error is MAD.

Author	Year	n	ϵ^{IMT} (µm)	Automatic
Liang et al. [21]	2000	50	42 $\pm$ 25	NO
Gutierrez et al. [17]	2002	30	90 $\pm$ 60	NO
Stein et al. [40]	2005	50	40 $\pm$ 7	NO
Faita et al. [10]	2008	150	10 $\pm$ 35	NO
Molinari et al. [29]	2010	182	54 $\pm$ 35	YES
Xu et al. [46]	2012	50	38.1 $\pm$ 16.4	NO

inter-observer error (-92 µm). Moreover, the dispersion of differences between A and GT with respect to the average (SD = 36 µm) is comparable to that of the intra-observer error (SD = 35.5 µm) and significantly lower than that of the inter-observer error (SD = 51.5 µm).

4 Conclusions

This paper proposes a segmentation method of the carotid far wall using neural networks in order to measure the Intima-Media Thickness (IMT) in a totally automatic way. The main advantage of our method is not only the automation but also the capability to automatically identify the most clearer sections on which the IMT measurements are performed. This ability allows the successful segmentation of noisy and blurred images even if the IMT boundaries are not visible along the whole longitudinal direction of the image.

The fundamental part of the proposed method is a classification stage. Segmentation is treated as a pattern recognition problem in which a Multi-Layer Perceptrons (MLP) must perform a binary classification of the pixels to find the IMT contours. For this purpose, different nets were trained under the Scaled Conjugate Gradient (SCG) learning method. Input patterns consist of the intensity values from a neighbourhood (windowing process) of the current pixel to be classified and different window sizes have been analysed. With the aim of improving the accuracy of this task, the results from three different MLP have been combined in a second stage by means of another MLP. This network ensemble has proven to be the best of all possible combinations of MLP for this application in particular. Our system is completed with a pre-processing stage in which the ROI is automatically selected and with a post-processing stage that takes charge of the extraction of the final boundaries starting from the results of the classification stage.

The proposed configuration of the system has been tested using a set of 60 ultrasound images of the CCA. Our segmentation method achieves the correct detection of the LI and MA interfaces in all the tested images. Several quantitative evaluations have showed its accuracy and robustness by comparing the obtained results with four manual segmentations. In this sense, the suggested approach stands out for the considerably reduction in the segmentation error for the MA interface which, generally, is the most difficult to segment.

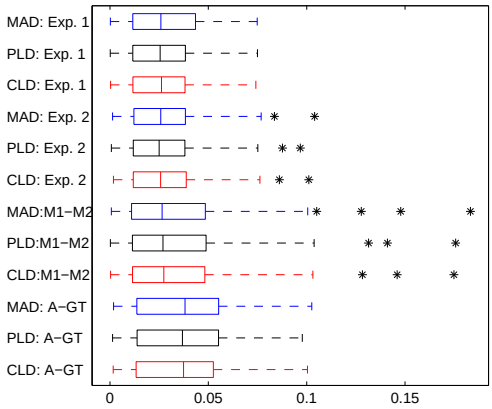

Fig. 27 Statistical distribution of the IMT measurement error between different segmentations using MAD, PLD and CLD metrics (mm).

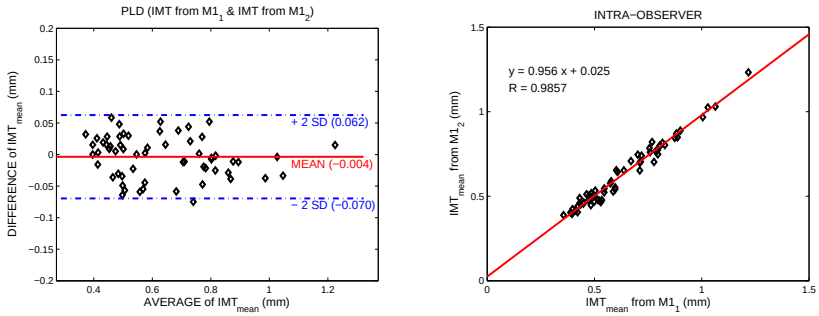

Fig. 28 Intra-observer measurement error. Statistical evaluation of IMT_{PLD} between $M1_1$ and $M1_2$: (left) Bland-Altman plot; (right) Regression analysis.

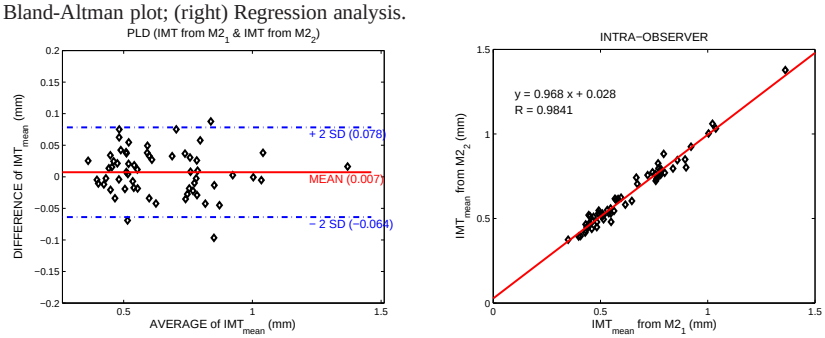

Fig. 29 Intra-observer measurement error. Statistical evaluation of IMT_{PLD} between $M2_1$ and $M2_2$: (left) Bland-Altman plot; (right) Regression analysis.

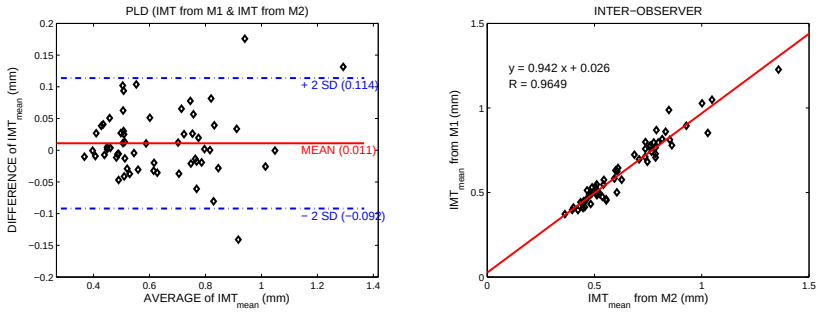

Fig. 30 Inter-observer measurement error. Statistical evaluation of IMT_{PLD} between M1 and M2: (left) Bland-Altman plot; (right) Regression analysis.

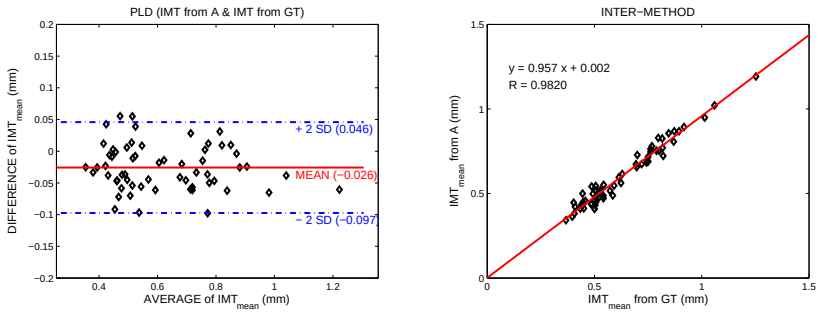

Fig. 31 Inter-method measurement error. Statistical evaluation of IMT_{PLD} between A and GT: (left) Bland-Altman plot; (right) Regression analysis.

Finally, we conclude that the application of pattern recognition techniques in the form suggested in this work is suitable for the clinical evaluation of IMT, because of the computational efficiency of the proposed procedure and the high agreement between automatic and manual segmentations. Future works could be focussed on also detecting the carotid near wall by the same strategy in order to measure the lumen diameter. Moreover, an adaptation of our method for the recognition of plaques may be of great interest.

Acknowledgements This work is partially supported by the Spanish Ministerio de Ciencia e Innovación, under grant TEC2009-12675. The images used and the anatomical knowledge have been provided by the radiology department of Hospital Universitario Virgen de la Arrixaca, Murcia, Spain.

References

1. Bastida-Jumilla, M.C., Menchón-Lara, R.M., Morales-Sánchez, J., Verdú-Monedero, R., Larrey-Ruiz, J., Sancho-Gómez, J.L.: Segmentation of the common carotid artery walls based on a frequency implementation of active contours. Journal of Digital Imaging **26**(1), 129–139 (2013). DOI 10.1007/s10278-012-9481-7
2. Bishop, C.M.: Pattern Recognition and Machine Learning. Springer (2006)
3. Bots, M., Evans, G.W., Riley, W., Grobbee, D.: Carotid intima-media thickness measurements in intervention studies: design options, progression rates, and sample size considerations: a point of view. Stroke **34**(12), 2985–2994 (2003)
4. Ceccarelli, M., De Luca, N., Morganella, A.: An active contour approach to automatic detection of the intima-media thickness. In: 2006 IEEE International Conference on Acoustics, Speech and Signal Processing. ICASSP 2006 Proceedings., vol. 5, pp. 709–712 (2006). DOI 10.1109/ICASSP.2006.1660441
5. Chan, R., Kaufhold, J., Hemphill, L., Lees, R., Karl, W.: Anisotropic edge-preserving smoothing in carotid b-mode ultrasound for improved segmentation and intima-media thickness (imt) measurement. In: Computers in Cardiology 2000, pp. 37–40 (2000). DOI 10.1109/CIC.2000.898449
6. Cheng, D.C., Jiang, X.: Detections of arterial wall in sonographic artery images using dual dynamic programming. Information Technology in Biomedicine, IEEE Transactions on **12**(6), 792 –799 (2008). DOI 10.1109/TITB.2008.926413
7. Cheng, D.C., Schmidt-Trucksass, A., Cheng, K.S., Burkhardt, H.: Using snakes to detect the intimal and adventitial layers of the common carotid artery wall in sonographic images. Computers Methods and Programs in Biomedicine **67**(1), 27–37 (2002)
8. Delsanto, S., Molinari, F., Giusetto, P., Liboni, W., Badalamenti, S., Suri, J.: Characterization of a completely user-independent algorithm for carotid artery segmentation in 2-d ultrasound images. IEEE Transactions on Instrumentation and Measurement **56**(4), 1265–1274 (2007)
9. Destrempes, F., Meunier, J., Giroux, M.F., Soulez, G., Cloutier, G.: Segmentation in ultrasonic b-mode images of healthy carotid arteries using mixtures of nakagami distributions and stochastic optimization. Medical Imaging, IEEE Transactions on **28**(2), 215 –229 (2009). DOI 10.1109/TMI.2008.929098
10. Faita, F., Gemignani, V., Bianchini, E., Giannarelli, C., Ghiadoni, L., Demi, M.: Real-time measurement system for evaluation of the carotid intima-media thickness with a robust edge operator. Journal of ultrasound in medicine **27**(9), 1353–1361 (2008)
11. Giacinto, G., Roli, F.: Desing of effective neural network ensembles for image classification purposes. Image and Vision Computing **19**(9-10), 699–707 (2001). DOI 10.1016/S0262-8856(01)00045-2
12. Golemati, S., Stoitsis, J., Sifakis, E.G., Balkizas, T., Nikita, K.S.: Using of the hough transform to segment ultrasound images of longitudinal and transverse sections of the carotid artery. Ultrasound in Medicine & Biology **33**(12), 1918–1932 (2007)
13. Gonzá, R.C.: Digital Image Processing using Matlab. Pentice Hall (2004)
14. Gonzalez, J., Wood, J., Dorey, F.J., Wren, T.A.L., Gilsanz, V.: Reproducibility of carotid intima-media thickness measurements in young adults. Radiology **247**(2), 465–247 (2008)
15. González, R.C., Woods, R.E.: Digital Image Processing, 2nd edn. Prentice Hall (2002)
16. Gustavsson, T., Liang, Q., Wendelhag, I., Wikstrand, J.: A dynamic programming procedure for automated ultrasonic measurement of the carotid artery. In: Computers in Cardiology 1994, pp. 297–300 (1994). DOI 10.1109/CIC.1994.470190
17. Gutierrez, M., Pilon, P., Lage, S., Kopel, L., Carvalho, R., Furuie, S.: Automatic measurement of carotid diameter and wall thickness in ultrasound images. In: Computers in Cardiology, 2002, pp. 359 – 362 (2002). DOI 10.1109/CIC.2002.1166783

18. Huang, Y., Suen, C.: A method of combining multiple experts for the recognition of unconstrained handwritten numerals. Pattern Analysis and Machine Intelligence, IEEE Transactions on **17**(1), 90–94 (1995). DOI 10.1109/34.368145
19. Ilea, D., Whelan, P., Brown, C., Stanton, A.: An automatic 2d cad algorithm for the segmentation of the imt in ultrasound carotid artery images. In: Engineering in Medicine and Biology Society, 2009. EMBC 2009. Annual International Conference of the IEEE, pp. 515 –519 (2009). DOI 10.1109/IEMBS.2009.5333773
20. Lee, Y.B., Choi, Y.J., Kim, M.H.: Boundary detection in carotid ultrasound images using dynamic programming and a directional haar-like filter. Computers in Biology and Medicine **40**(8), 687 – 697 (2010). DOI 10.1016/j.compbiomed.2010.03.010
21. Liang, Q., Wendelhag, I., Wikstrand, J., Gustavsson, T.: A multiscale dynamic programming procedure for boundary detection in ultrasonic artery images. Medical Imaging, IEEE Transactions on **19**(2), 127–142 (2000). DOI 10.1109/42.836372
22. Liguori, C., Paolillo, A., Pietrosanto, A.: An automatic measurement system for the evaluation of carotid intima-media thicknesss. Instrumentation and Measurement, IEEE Transactions on **50**(6), 1684 –1691 (2001). DOI 10.1109/19.982968
23. Liu, G., Wang, B., Liu, D.: Detection of intima-media layer of common carotid artery with dynamic programming based active contour model. In: Pattern Recognition, 2008. CCPR '08. Chinese Conference on, pp. 1–6 (2008). DOI 10.1109/CCPR.2008.78
24. Loizou, C., Pantziaris, M., Pattichis, M., Kyriacou, E., Pattichis, C.: Ultrasound image texture analysis of the intima and media layers of the common carotid artery and its correlation with age and gender. Computerized Medical Imaging and Graphics **33**(4), 317–324 (2009). DOI 10.1016/j.compmedimag.2009.02.005
25. Loizou, C.P., Pattichis, C.S., Pantziaris, M., Tyllis, T., Nicolaides, A.: Snakes based segmentation of the common carotid artery intima media. Medical and biological engineering and computing **45**(1), 35–49 (2007). DOI 10.1007/s11517-006-0140-3
26. Meyer, F.: Topographic distance and watershed lines. Signal Processing **38**(1), 113–125 (1994)
27. Meyer-Base, A.: Pattern Recognition for Medical Imaging. Academic Press (2004)
28. Molinari, F., Meiburger, K.M., Saba, L., Acharya, U.R., Ledda, M., Nicolaides, A., Suri, J.S.: Constrained snake vs. conventional snake for carotid ultrasound automated imt measurements on multi-center data sets. Ultrasonics **52**(7), 949 – 961 (2012). DOI 10.1016/j.ultras.2012.03.005
29. Molinari, F., Zeng, G., Suri, J.: Intima-media thickness: setting a standard for a completely automated method of ultrasound measurement. Ultrasonics, Ferroelectrics and Frequency Control, IEEE Transactions on **57**(5), 1112–1124 (2010). DOI 10.1109/TUFFC.2010.1522
30. Molinari, F., Zeng, G., Suri, J.S.: Review: A state of the art review on intima-media thickness (imt) measurement and wall segmentation techniques for carotid ultrasound. Comput. Methods Prog. Biomed. **100**(3), 201–221 (2010). DOI 10.1016/j.cmpb.2010.04.007
31. Moller, M.: A scaled conjugate gradient algorithm for fast supervised learning. Neural Networks **6**, 525–533 (1993)
32. Moré, J.J.: The levenberg-marquardt algorithm: Implementation and theory. In: G. Watson (ed.) Numerical Analysis, *Lecture Notes in Mathematics*, vol. 630, pp. 105–116. Springer Berlin Heidelberg (1978). DOI 10.1007/BFb0067700
33. Organization, W.H.: Global atlas on cardiovascular disease prevention and control. online. URL www.who.int/cardiovascular_diseases/en/
34. Pham, D., Xu, C., Prince, J.: Current methods in medical image segmentation. Annual Review of Biomedical Engineering **2**, 315–337 (2000). DOI 10.1146/annurev.bioeng.2.1.315
35. Rocha, R., Campilho, A., Silva, J., Azevedo, E., Santos, R.: Segmentation of the carotid intima-media region in b-mode ultrasound images. Image and Vision Computing **28**(4), 614–625 (2010)
36. Santhiyakumari, N., Madheswaran, M.: Non-invasive evaluation of carotid artery wall thickness using improved dynamic programming technique. Signal, Image and Video Processing **2**(2), 183–193 (2008). DOI 10.1007/s11760-007-0048-x
37. Schmidt-Trucksass, A., Cheng, D.c., Sandrock, M., Schulte-Monting, J., Rauramaa, R., Huonker, M., Burkhardt, H.: Computerized analysing system using the active contour in ultrasound measurement of carotid artery intima-media thickness. Clinical Physiology **21**(5), 561–569 (2001). DOI 10.1046/j.1365-2281.2001.00358.x
38. Selzer, R.H., Mack, W.J., Lee, P.L., Kwong-Fu, H., Hodis, H.N.: Improved common carotid elasticity and intima-media thickness measurements from computer analysis of sequential ultrasound frames. Atherosclerosis **154**(1), 185 – 193 (2001). DOI 10.1016/S0021-9150(00)00461-5
39. Sheehan, F.H., Stewart, D.K., Dodge, H.T., Mitten, S., Bolson, E.L., Brown, B.G.: Variability in the measurement of regional left ventricular wall motion from contrast angiograms. Circulation **68**(3), 550–559 (1983)

40. Stein, J.H., Korcarz, C.E., Mays, M.E., Douglas, P.S., Palta, M., Zhang, H., LeCaire, T., Paine, D., Gustafson, D., Fan, L.: A semiautomated ultrasound border detection program that facilitates clinical measurement of ultrasound carotid intima-media thickness. Journal of the American Society of Echocardiography **18**(3), 244–251 (2005). DOI 10.1016/j.echo.2004.12.002
41. Suri, J.S., Haralick, R.M., Sheehan, F.H.: Greedy algorithm for error correction in automatically produced boundaries from low contrast ventriculograms. Pattern Analysis & Applications **3**(1), 39–60 (2000). DOI 10.1007/s100440050005
42. Touboul, P.J., Hennerici, M., Meairs, S., Adams, H., Amarenco, P., Bornstein, N., Csiba, L., Desvarieux, M., Ebrahim, S., Hernandez Hernandez, R., Jaff, M., Kownator, S., Naqvi, T., Prati, P., Rundek, T., Sitzer, M., Schminke, U., Tardif, J.C., Taylor, A., Vicaut, E., Woo, K.: Mannheim carotid intima-media thickness and plaque consensus (2004-2006-2011). Cerebrovascular Diseases **34**, 290–296 (2012). DOI 10.1159/000343145
43. Velázquez, F., Berná, J.D., Abellán, J.L., Serrano, L., Escribano, A., Canteras, M.: Reproducibility of sonographic measurements of carotid intima-media thickness. Acta Radiologica **49**(10), 1162–1166 (2008). DOI 10.1080/02841850802438520
44. Wendelhag, I., Liang, Q., Gustavsson, T., Wikstrand, J.: A new automated computerized analysis system simplifies readings and reduces the variability in ultrasound measurement of intima-media thickness. Stroke **28**, 2195–2200 (1997)
45. Xu, L., Krzyzak, A., Suen, C.: Methods of combining multiple classifiers and their applications to handwriting recognition. Systems, Man and Cybernetics, IEEE Transactions on **22**(3), 418–435 (1992). DOI 10.1109/21.155943
46. Xu, X., Zhou, Y., Cheng, X., Song, E., Li, G.: Ultrasound intima-media segmentation using hough transform and dual snake model. Computerized Medical Imaging and Graphics **36**(3), 248–258 (2012). DOI 10.1016/j.compmedimag.2011.06.007